Measurement with microscopic MRI and simulation of flow in different aneurysm models

Daniel Edelhoff[a)]
Experimental Physics III, TU Dortmund University, Otto-Hahn-Street 4, Dortmund 44227, Germany

Lars Walczak
Computer Science VII, TU Dortmund University, Otto-Hahn-Street 16, Dortmund 44227, Germany

Frauke Frank[b)] and Marvin Heil
Experimental Physics III, TU Dortmund University, Otto-Hahn-Street 4, Dortmund 44227, Germany

Inge Schmitz
Institute for Pathology, Ruhr Universität Bochum, Bürkle-de-la-Camp-Platz 1, Bochum 44789, Germany

Frank Weichert
Computer Science VII, TU Dortmund University, Otto-Hahn-Street 16, Dortmund 44227, Germany

Dieter Suter
Experimental Physics III, TU Dortmund University, Otto-Hahn-Street 4, Dortmund 44227, Germany

(Received 8 January 2015; revised 12 August 2015; accepted for publication 17 August 2015; published 8 September 2015)

Purpose: The impact and the development of aneurysms depend to a significant degree on the exchange of liquid between the regular vessel and the pathological extension. A better understanding of this process will lead to improved prediction capabilities. The aim of the current study was to investigate fluid-exchange in aneurysm models of different complexities by combining microscopic magnetic resonance measurements with numerical simulations. In order to evaluate the accuracy and applicability of these methods, the fluid-exchange process between the unaltered vessel lumen and the aneurysm phantoms was analyzed quantitatively using high spatial resolution.
Methods: Magnetic resonance flow imaging was used to visualize fluid-exchange in two different models produced with a 3D printer. One model of an aneurysm was based on histological findings. The flow distribution in the different models was measured on a microscopic scale using time of flight magnetic resonance imaging. The whole experiment was simulated using fast graphics processing unit-based numerical simulations. The obtained simulation results were compared qualitatively and quantitatively with the magnetic resonance imaging measurements, taking into account flow and spin–lattice relaxation.
Results: The results of both presented methods compared well for the used aneurysm models and the chosen flow distributions. The results from the fluid-exchange analysis showed comparable characteristics concerning measurement and simulation. Similar symmetry behavior was observed. Based on these results, the amount of fluid-exchange was calculated. Depending on the geometry of the models, 7% to 45% of the liquid was exchanged per second.
Conclusions: The result of the numerical simulations coincides well with the experimentally determined velocity field. The rate of fluid-exchange between vessel and aneurysm was well-predicted. Hence, the results obtained by simulation could be validated by the experiment. The observed deviations can be caused by the noise in the measurement and by the limited resolution of the simulation. The resulting differences are small enough to allow reliable predictions of the flow distribution in vessels with stents and for pulsed blood flow. [http://dx.doi.org/10.1118/1.4929758]

Key words: MRI, ToF, aneurysm, lattice Boltzmann method, 3D printing

1. INTRODUCTION

The principles for measuring fluid velocity by magnetic resonance imaging (MRI) have been known since the 1960s.[1] The main techniques, known as time of flight (ToF)[2–4] and phase contrast (PC),[5] are used for various medical as well as technically relevant applications.[6–8] The ToF technique is mainly used for visualizations of flow processes and for an intuitive way to understand flow behavior. In clinical applications, arteries can be visualized and flowing blood can be tracked.[9] The techniques have been improved by recent technical developments, such as higher magnetic fields and higher gradient strengths, resulting in higher signal-to-noise ratios and better spatial resolution down to microscopic scales. Microscopic imaging was used by Aguayo *et al.*[10] and was transferred to the flow techniques,[11,12] though both are still

areas of recent research.[13–15] Moreover, new low-field setups allow one to assess useful flow information in medically relevant contexts.[16]

Accurate knowledge of flow behavior is helpful for understanding the development of cardiovascular diseases and estimating risks of complications, such as stenosis and aneurysm growth and rupture. Vessel ruptures are associated with high mortality.[17]

Computational fluid dynamics (CFD) is gaining acceptance for biomedical purposes, as it provides relatively effortless access to various fluid models and geometries, compared to model building and real measurements. Nevertheless, CFD needs validation. Especially in complex 3D geometries and for realistic flows, it is still a challenge to validate the simulations. Experimentally measured velocities within different sample geometries have been compared to different types of CFD simulations (lattice Boltzmann being one of them) in earlier studies.[13,18–22] Here, we apply a new coupled multigrid LBM model for fluid flow and spin transport, including spin–lattice relaxation, and validate the simulated mass transport.

Recently, the model-building process for flow experiments was simplified with the introduction of affordable 3D printers. Combined with 3D modeling of aneurysm phantoms inside a flow apparatus, this provides access to new ways of measuring flow in complicated yet controllable geometries.

MRI measurements may contain measurement artifacts, such as phase accumulation from higher-order moments of the gradients, velocity averaging in a recorded slice, spin flow out of a slice, or susceptibility differences between fluid and wall.[23] Additionally, impurities in the fluid, asymmetries in the experimental setup, unknown temperature influences, or other aspects can affect the measurements. Accordingly, a detailed comparison of high-resolution experimental and numerical data is important for validating both types of data.

In the present study, we analyze microscopic ToF measurements and corresponding CFD simulations in order to test precision limits and the applicability of both techniques. We focus on deviations between the measurement and simulation and the validation of the simulation method. Within the used aneurysm model geometries, we also characterize the fluid-exchange and propose a method for quantification. The numerical simulation takes spin–lattice relaxation of the nuclear spins into account. This allows a quantitative comparison between measured and simulated data. In this study, we exclude the effect of pulsatile flow and the non-Newtonian fluid behavior of blood. This avoids complications of safety and ethical issues of using blood.

2. METHODS

2.A. Pulse sequences

2.A.1. Time of flight with planar labeling

ToF MRI labels selected volumes by modifying their spin polarization and tracking the labeled spins over time. For the tagging step, we combine radio frequency (RF) pulses with magnetic field gradients to saturate the spins in a selected plane. After the tagging step and a suitable delay, during which the tagged spins are transported by the flow, the resulting distribution of the spin polarization is imaged by a gradient echo sequence, typically a FLASH sequence.[24] If only one plane is to be labeled, this can be achieved by a frequency-selective sinc-pulse in a magnetic field gradient that is applied perpendicular to the plane. The carrier frequency and duration of the pulse determine position and width of the selected slice, together with the gradient strength. Figure 1 shows this pulse sequence. The tagging step can be performed for two or more different areas. Each area has its individual evolution time.

2.B. Model and numerical methods

In order to compare the measurements obtained by our experimental setup, we had to derive a suitable model and numerics for simulation. In its partial differential equation form, writing $\vec{x}$ for position and t for time, the evolution of the longitudinal magnetization M_z, given a fluid-flow velocity

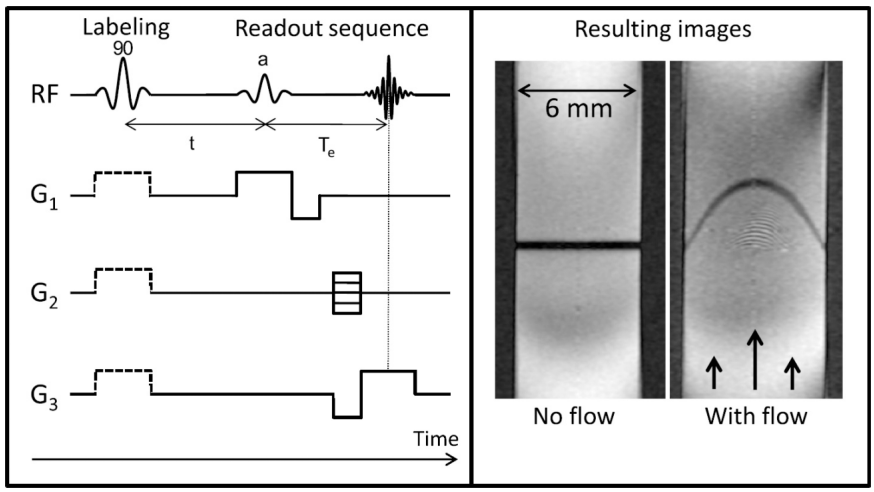

FIG. 1. Schematic representation of the pulse sequence. After the labeling with a frequency-selective RF pulse, a FLASH sequence images the volume of interest.

field $\vec{u}$, can be described by the following equation:

$$\frac{\partial M_z}{\partial t} + \vec{u}\cdot\nabla M_z = D\frac{\partial^2 M_z}{\partial \vec{x}^2} - \frac{M_z - M_0}{T_1}, \quad (1)$$

where M_0 is the thermal equilibrium value of the nuclear spin magnetization, T_1 the spin–lattice relaxation time, and D the selfdiffusion coefficient.

To simulate the whole process consisting of fluid dynamics, spin transport, and spin relaxation, a multigrid LBM approach was used to separate the fluid dynamics problem from the magnetization evaluation. The first grid for solving the fluid dynamics problem is described in detail in Edelhoff *et al.*,[13] but it was modified in this context by using a two-relaxation-time [TRT (Refs. 25 and 26)] LB model. The second grid is coupled with the simulated velocity field $\vec{u}$ of the fluid dynamics part and solves for the transport and relaxation of the magnetization described by Eq. (1). The used lattice model is abbreviated as $D3Q7$ in the usual notation. The seven directions are $\vec{e}_0 = (0,0,0)$, $\vec{e}_{\{1,\ldots,6\}} = \{(\pm c,0,0),(0,\pm c,0),(0,0,\pm c)\}$, where $c = \delta x/\delta t$ is the lattice velocity with δx being the lattice spacing and δt the time step. The corresponding weighting factors are $w_0 = 1/4$ and $w_{\{1,\ldots,6\}} = 1/8$. The nuclear spin magnetization M_z is obtained by summing up the probability distribution functions (PDFs) m_i corresponding to the directions $\vec{e}_i$. The larger m_i is, the more magnetization is transported in direction $\vec{e}_i$. The sum of all PDFs $M_z(\vec{x},t) = \sum_{i=0}^{6} m_i(\vec{x},t)$ describes the magnetization at position $\vec{x}$ and at time t.

The LBM evolution equation can be written as

$$m_i(\vec{x}+\vec{e}_i\delta t, t+\delta t) - m_i(\vec{x},t) = \Omega_{\mathrm{CD}}(\vec{x},t) + \Omega_R(\vec{x},t). \quad (2)$$

Here, the right-hand side of the equation is modified in comparison to the previous study.[13] We use two collision operators (Ω_{CD} and Ω_R) to describe the process. The first collision operator Ω_{CD} describes the effect of convection and diffusion, while the second operator Ω_R summarizes the relaxation process.

The convection–diffusion collision operator

$$\Omega_{\mathrm{CD}}(\vec{x},t) = -\frac{m_i^s(\vec{x},t) - m_i^{s\mathrm{eq}}(M_z(\vec{x},t),\vec{u}(\vec{x},t))}{\tau_s} - \frac{m_i^a(\vec{x},t) - m_i^{a\mathrm{eq}}(M_z(\vec{x},t),\vec{u}(\vec{x},t))}{\tau_a} \quad (3)$$

uses the TRT model.[27–29] It is separated in the symmetric (superscript "s") and antisymmetric (superscript "a") parts of the distribution typically used in the TRT scheme. The symmetric and antisymmetric particle distribution functions can be written as $m_i^s = (m_i + m_{\bar{i}})/2$ and $m_i^a = (m_i - m_{\bar{i}})/2$, while $\bar{i}$ indicates the opposite direction to i. The equilibrium distribution functions can be written as $m_i^{s\mathrm{eq}} = (m_i^{\mathrm{eq}} + m_{\bar{i}}^{\mathrm{eq}})/2$ and $m_i^{a\mathrm{eq}} = (m_i^{\mathrm{eq}} - m_{\bar{i}}^{\mathrm{eq}})/2$. The equilibrium distribution functions m_i^{eq} can be read in linear form as follows:[29]

$$m_i^{\mathrm{eq}} = w_i M_z\left(1 + \frac{4}{c^2}\vec{e}_i\cdot\vec{u}\right), \quad i = 0,\ldots,6. \quad (4)$$

Both the symmetric and antisymmetric parts are relaxed independently using the TRT method. The antisymmetric relaxation time τ_a in Eq. (3) is set according to the diffusion coefficient

$$D = \frac{1}{4}\left(\tau_a - \frac{1}{2}\right)\frac{\delta x^2}{\delta t}. \quad (5)$$

The symmetric relaxation time τ_s is set according to the relation

$$\Lambda = \left(\tau_s - \frac{1}{2}\right)\left(\tau_a - \frac{1}{2}\right), \quad (6)$$

where Λ offers a tunable parameter that can be used, e.g., to improve stability of the simulation.[30]

The second collision operator models the Bloch-like term of Eq. (1),

$$\Omega_R(\vec{x},t) = -\frac{m_i(\vec{x},t) - m_i^0}{T_1'}. \quad (7)$$

The term T_1' in the equation represents the T_1 time in lattice time units δt. Finally, $m_i^0 = w_i M_0$ stands for the part of M_0 that applies to direction $\vec{e}_i$.

2.C. Parameterization of multigrid LBM systems to physical reference values

The CFD part itself is parameterized like in a previous work,[13] by taking the TRT model into account. We used the velocity field from a 2D phase contrast measurement,[5] as described in the previous study[13] to be the inlet velocity boundary condition.

Regarding the spin transport and T_1 relaxation, the initial conditions for M_z in the tagged 2D slice of the 3D grid are obtained from the first 2D measurement. The values can be set either to the noisy spin densities derived from the RF signal or to a suitable quantization of these, ideally set to $M_z = 0$ for tagged cells. The remaining 3D lattice nodes are set to a normalized value of $M_z = M_0 = 1$. The boundary conditions at the inlet and outlet as well as at the boundaries are similar to what was described previously in the CFD case.[13] The inlet boundary condition is set to M_0. The relaxation time T_1 was measured during the experiment and T_1' is set accordingly.

What remains to be described is the coupling of both grids. The Peclet number $Pe = c_L c_U/D$ is a dimensionless number describing the ratio of convective and diffusive transport. The selfdiffusion coefficient of water $D = D_{\mathrm{H_2O}}$ is given, and the characteristic length c_L and characteristic velocity c_U are known from the CFD part; therefore, Pe is fixed. Using the same grid resolution δx as in the CFD case, the only variables in Eq. (5) are δt and τ_a. For positive diffusion coefficients $D > 0$, δt is limited by $\tau_a > 1/2$. We choose δt as an integer multiple k of its CFD counterpart while satisfying $\tau_a > 1/2$ and the stability of the second grid. In a dynamic simulation (e.g., pulsatile flows), for every CFD step k, mass transport steps have to be done (or vice versa). If the values permit, $k = 1$ should be favored. For a steady flow field like in this case, the CFD simulation can be solved until the steady state is reached and then the mass transport can take over. For stability reasons, following Ginzburg *et al.*,[30] the magic number $\Lambda = 1/4$ is chosen to determine τ_s in Eq. (6).

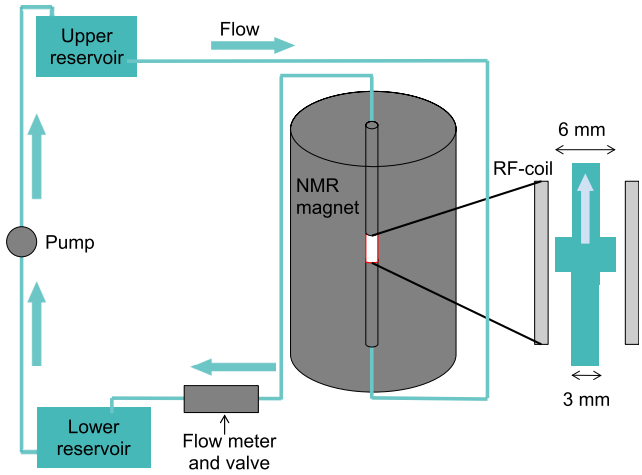

FIG. 2. Schematic representation of the used experimental flow setup.

3. EXPERIMENTAL SETUP AND PARAMETERS

3.A. Experiment

The microscopic MRI measurements were performed in a wide-bore magnet with a magnetic field strength of 14.1 T. The used magnetic field gradient system provides a strength of up to 1 T/m, which led to high spatial resolutions in the order of 10 μm for the applied imaging sequences. A 10 mm RF-insert was combined with a home-built probe. The probe is accessible from both sides and allows flow measurements with 3D-printed phantoms. A scheme of the experimental setup is shown in Fig. 2. We used a reservoir above the magnet, refilled by the circulation pump, to provide a constant hydrostatic pressure in the tube system. The flow rate was monitored by an inductive flow counter and adjusted by a proportional valve. The used liquid was distilled water (temperature 20 °C) with 0.12% copper sulfate added to reduce the T_1 time of the sample to 870 ms. All connections between the components consisted of PVC tubes.

3.B. Simulation

We implemented the multigrid LBM simulation described above on an asynchronous multi-graphics processing unit (GPU) system. Two approaches were explored. First, each LBM grid lived on its own GPU and communicated the velocity field through the system's PCI-Express bus in a copy-and-forget fashion from one GPU solving the CFD part to the other. Second, the simulation domain was cut into two parts, depending on the relative performance and the memory sizes of the GPUs. Both GPUs executed both LBM grids on their part of the data set and synchronized the boundary PDFs with each other. Although one could efficiently hide the data transfers in the first approach with asynchronous memory transfers, the latter was more efficient because less data had to be transferred over the system's bus, but it was harder to implement. Using both techniques, we could simulate spin transport and spin–lattice relaxation in time-varying flows. In a steady flow scenario like in this case, the velocity field had to be calculated (and if required transferred) only once. Compared to Edelhoff *et al.*,[13] the memory of both GPUs could be used fully without the need for swapping the different sets of PDFs of the two grids over the bus at every time step.

The selfdiffusion coefficient D_{H_2O} was set to $2 \cdot 10^{-9}$ m^2/s, corresponding to the water temperature of 20 °C. However, because D_{H_2O} led to values of τ_a that were close to the stability limit of 1/2 using the CFD grid parameterization for spin transport, there were stability problems using a single-relaxation-time (SRT) LB model. We opted for the two-relaxation-time model, which allows one to parameterize the simulation using the physical selfdiffusion coefficient. The resulting flows were strongly convection-dominated in the main tubes. In the aneurysm or widened tube parts, diffusion effects could be expected because of the significantly lower flow velocities in these areas.

4. RESULTS

4.A. Geometries

The measurements were carried out in two different geometries to verify the simulations. The used models were generated by a "MakerBot Replicator 2" 3D printer (MakerBot Industries, LLC, Brooklyn, NYC) and consisted of polylactide. The prints are called models "A" and "B" in the following. Model geometry A consists of a symmetric transition from 2.4 to 4.8 to 2.4 mm diameter and the reconstructed geometry of MRI data is shown in Fig. 3. This reconstructed geometry was used as boundary condition for the simulation. Furthermore, the velocity distribution of the first slice on the inflowing side was used as the inlet boundary condition for the simulation. The boxed areas in the extensions show the labeled slices for the excitation in ToF measurement. The blue slice represents the imaging plane for the ToF measurement. A rendering for the printed expansion model including the supplies is shown in Fig. 4 (left-hand side) (Multimedia view). The main tube is 10 mm in diameter, while the top part for holding the model in place inside the RF coil is 35 mm in diameter. The overall height is 125 mm. To connect the model with the tube system of

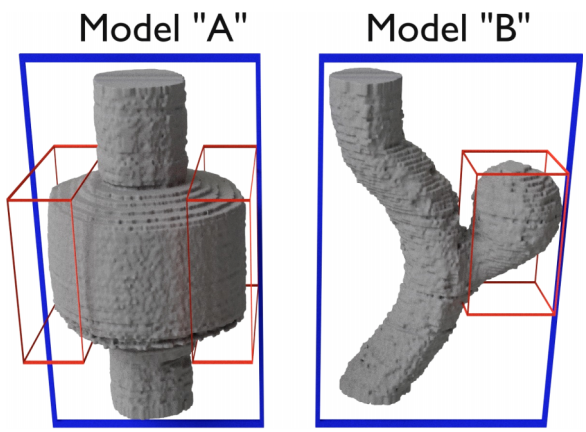

FIG. 3. Model A: image of the 2.4–4.8–2.4 mm printed geometry. Model B: image of the printed aneurysm.

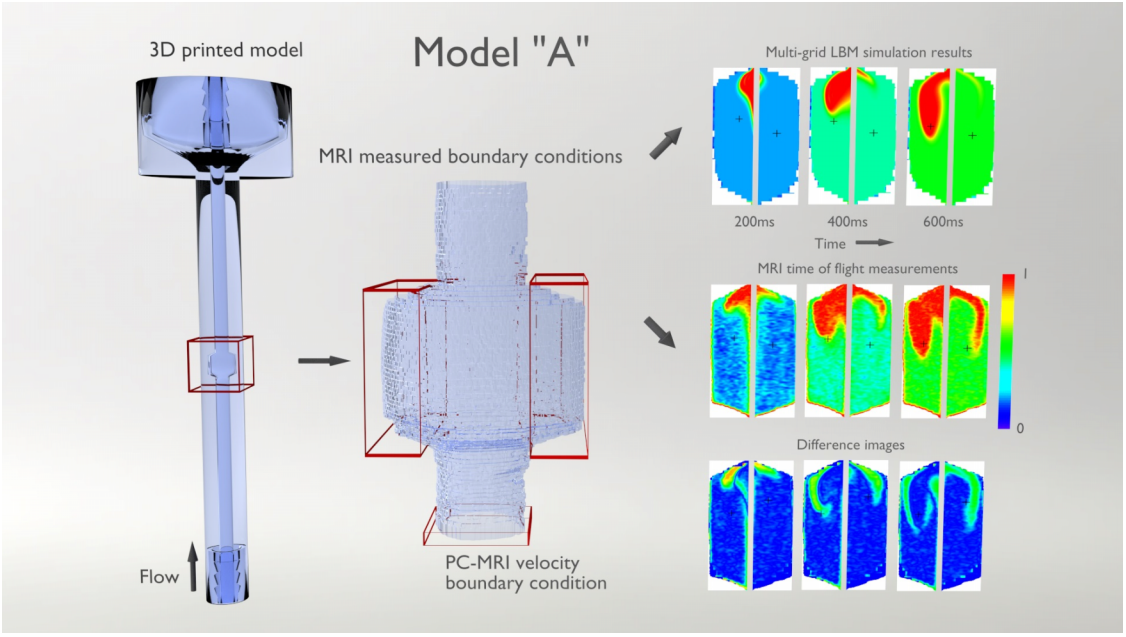

FIG. 4. Model A: On the left, a rendered view of the 3D model used for 3D printing is shown. In the middle, the MRI measurement for setting up the boundary conditions for the simulation is presented. On the right, a comparison of simulation (top row), measurement (middle row), and difference (bottom row) at time 200, 400, and 600 ms for the different regions is shown. In the top and middle row the colors depict the concentration of the spins (1 stands for fresh spins), whereas the colors in the bottom row depict the difference in percent. (Multimedia view) [URL: http://dx.doi.org/10.1118/1.4929758.1]

the experimental flow setup, two fittings are located at the top and the bottom. The expansion is located in the gradient unit.

The second geometry B was inspired by a pathological vessel that formed an aneurysm and was used in a previous study[31] to compare different numerical simulations. The reconstructed geometry from MRI data is also shown in Fig. 3. Again, the labeled area is marked by a box. A rendering for the printed aneurysm model including the supplies is shown in Fig. 5 (left-hand side) (Multimedia view). The main geometry of the printed model is identical to model A, but the curved inflowing and out-flowing tubes connecting the fittings with the aneurysm are modeled with smooth nonuniform rational B-splines (NURBS) curves. The aneurysm part is positioned in such a way that it is placed precisely inside the gradient unit.

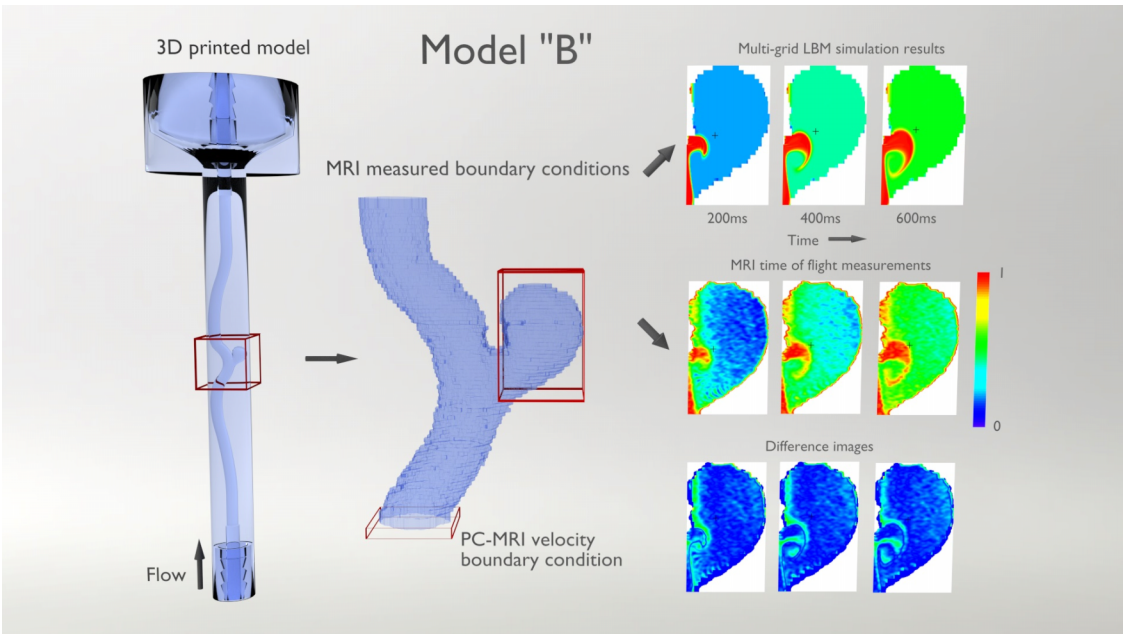

FIG. 5. Model B: On the left, a rendered view of the 3D model used for 3D printing is shown. In the middle, the MRI measurement for setting up the boundary conditions for the simulation is shown. On the right, a comparison of simulation (top row), measurement (middle row), and difference (bottom row) at time 200, 400, and 600 ms is presented. In the top and middle row the colors depict the concentration of the spins (1 stands for fresh spins), whereas the colors in the bottom row depict the difference in percent. (Multimedia view) [URL: http://dx.doi.org/10.1118/1.4929758.2]

For both models, we used the highest possible printer resolution of 100 μm in the z-direction and according to the specifications of the printer $\approx$10 μm positioning accuracy in the x–y-plane.

4.B. Measurement and simulation results

Sections 4.B.1 and 4.B.2 describe the results of the ToF measurements as well as the corresponding simulations. For all models, the simple ToF technique described in Sec. 2.A.1 was used to tag the extension and observe the fluid-exchange behavior over time. Therefore, images with varying times τ_1 and τ_2 corresponding to the different extensions were acquired and the evolution of the tagged areas was observed. The tagged areas as well as the imaging plane are shown in Fig. 3. For the following images, we used a repetition time T_r of 4 s to be sure that the labeled area was relaxed before the next phase step. The echo time was set to $T_e = 21$ ms. The isotropic FOV of 9×9 mm in combination with the 256 phase steps and the same acquisition length led to a digital resolution of $17.5 \times 17.5 \times 150$ μm^3 (after zero filling and slice selection). The evolution time τ was increased by steps of 50 to 600 ms for the right tagged area, while the left tagged area was labeled 1.5 ms earlier.

The simulation grid size varies for the models; therefore, all necessary information for the geometries is summarized in Table I.

4.B.1. Model A

The right-hand side of Fig. 4 (Multimedia view) shows three example images for both tagged extensions. The tagged areas in the simulation as well as in the measurement start with a small signal, while the untagged spins generate a larger signal close to one. The signal increase due to the T_1 relaxation is clearly visible for longer evolution times. The observed flow behavior in the simulation as well as in the measurement shows a strong asymmetric exchange between the vessel and the two extensions. The left extension shows a large vortex that takes almost half the extension after 600 ms, while in the right extension, only a small finger of about one fourth the size develops. In addition to the measured images, the centers of mass of the areas are indicated with black crosses. The left-hand side of the figure shows the 3D-printed model.

4.B.2. Model B—Aneurysm

Figure 5 (Multimedia view) shows the results of the ToF measurements of the aneurysm model. We observed a tiny vortex development on the upper side of the aneurysm neck while an outflow takes place on the lower side after further evolution. The total exchange process only takes place in a small volume close to the inlet, which could lead to problems, e.g., the formation of a thrombosis. The overall behavior of the measurement and simulation is similar. In addition to the measured images, the centers of mass of the areas are indicated with black crosses.

4.C. Analysis of the fluid-exchange

For direct comparison between measurement and simulation, the tagged areas were analyzed. At first, the measurement and simulation results were regridded to the same size and then the filtered difference was calculated, by taking the mean value of nine pixels in both images and subtracting the simulated from the measured data. Only data belonging to both geometries were considered. At the boundaries, deviations were obvious due to the difference in the grid resolution. Furthermore, the ToF measurement was resolved much higher (17 μm) in the main flow direction than the geometry provided by the boundary condition measurement (150 μm), see Edelhoff *et al.*[13] For all differences and time evolutions, we refer to the supplemental videos (see Figs. 4 and 5). Moreover, the direct-differences histograms of the signal distribution for selected extensions were used to show the characteristics of the fluid-exchange.

4.C.1. Model A—3D-printed extension

For model A, the highest deviation between measurement and simulation is found in the right expansion. The filtered differences between the data lead to relative differences of (7 ± 11)% for 200 ms, (8 ± 13)% for 400 ms, and (11 ± 14)% for 600 ms evolution for the right expansion. We observe an

TABLE I. Summarizing table for characteristics of the analyzed models.

	Model A	Model B
Velocity v_{max} (cm/s)	7.1	5.8
Flow rate Q (l/h)	0.77	0.63
Digital resolution measurement (μm)	$17.5 \times 17.5 \times 150$	$17.5 \times 17.5 \times 150$
Resolution simulation (μm)	28.2^3	27.9^3
Grid size	$208 \times 216 \times 332$	$292 \times 124 \times 420$
Reynolds number Re	169.28	139.44
Peclet number Pe (main tube)	84 960	69 984
Geometry AABB[a] dimensions (mm)	$5.9 \times 6.1 \times 9.4$	$8.1 \times 3.5 \times 11.7$
Tube diameter (mm)	2.4	2.4

[a]AABB stands for axis aligned bounding box.

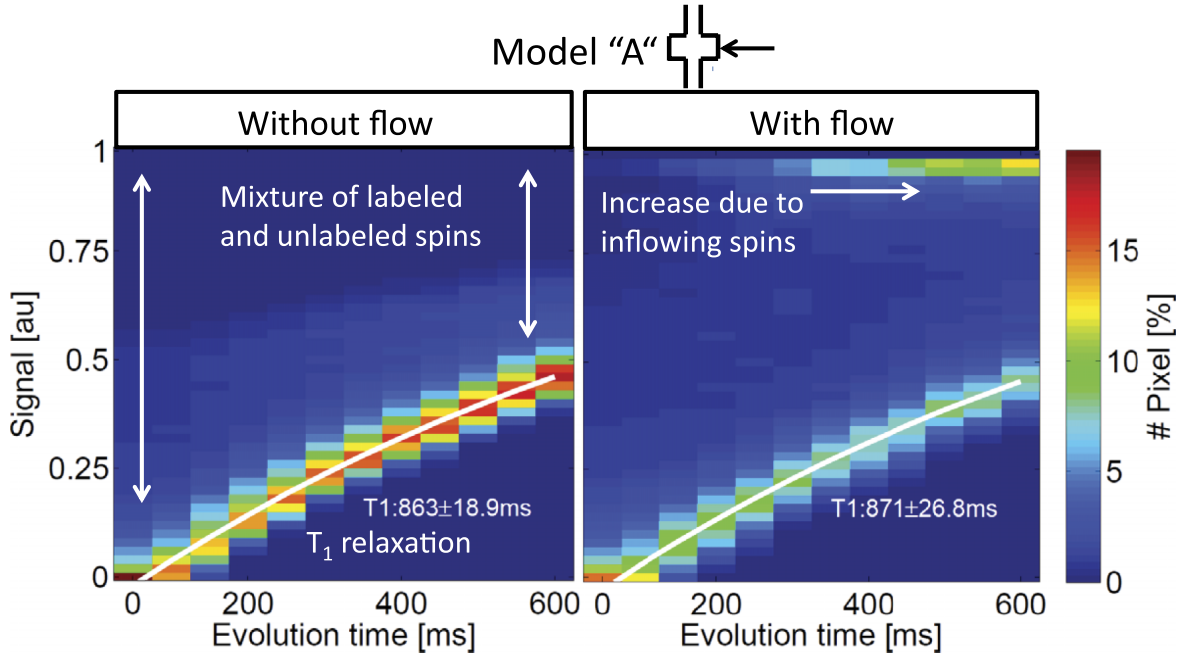

FIG. 6. Histograms of the signal distribution for the measured model A over time. The left-hand side shows the signal distribution for the right expansion without flow, while the right-hand side of the figure shows the distribution with flow.

increase of the deviation with longer evolution times, which is mainly caused by the smaller inflowing vortex in the simulation, compared to the one in the measurement; see video in the supplementary material. In the left extension, the deviation remains on the same level $(13 \pm 18)\%$ for 200 ms, $(12 \pm 16)\%$ for 400 ms, and $(11 \pm 14)\%$ for 600 ms evolution. Here, the observed deviation is dominated by the vortex that is located closer to the boundary in the measurement, as visible in Fig. 4 (Multimedia view). The SNR was 75 in these measurements and causes about 1% of this deviation.

In order to characterize the water exchange between the expansions and the rest of the measured slice of the shown ToF measurements, we use histograms. Each time evolution was measured additionally to the shown measurements without flow through the system. This serves as the reference signal, whose evolution represents the T_1 relaxation of the sample and diffusion processes. Figure 6 shows the resulting distribution of the signal amplitudes for model A, in right expansion. The main signal increase corresponds to the T_1 decay, which is visible in the nearly triangular shape of the distribution over time, while the border line can be seen as the nearly linear part of the exponential T_1 relaxation function of the sample (T_1 = 870 ms). In the images, a difference between the histograms with and without flow is clearly visible. The histogram for the measurement without flow is dominated by the T_1 relaxation and a Gaussian distribution around the value defined by the relaxation due to uncertainties in the excitation and noise in the measurement. In contrast to the steady histogram, the inflowing spins are visible on the right-hand side of the figure. A wider distribution of the signal is visible, especially with increasing evolution time. The mentioned difference between the behaviors increases for higher evolution times, when the distribution shifts from the decay line to pixels with higher intensity and the number of pixels with signal close to one increases. Those pixels correspond to fresh (unlabeled) inflowing water while pixels with a mixture of labeled and unlabeled water are distributed between the maximum value and the decay line. For higher evolution times, this area decreases and, therefore, also the resolution for the fluid-exchange analysis. The measured signal $S_{\text{meas}}(t)$ can be described by the following equation:

$$S_{\text{meas}}(t) = S_0(t) + S_{\text{flow}}(t). \tag{8}$$

$S_0(t) = (1 - e^{-t/T_1})$ is the signal due to the normal T_1 relaxation, which we obtain from the reference measurement without flow. $S_{\text{flow}}(t)$ is the signal due to the flow of fully polarized protons into the volume of interest. Comparing the quantities S_{meas} and S_0, we determined the fraction of liquid that has been exchanged.

The histogram comparison and the calculated fluid-exchange show the strong asymmetry between the two areas of interest. The left extension shows only a fluid-exchange of 6% according to the measurement and 4% according to the simulation. This difference between simulation and measurement is caused by the smaller vortex from the simulation data. In contrast, the left expansion shows a big fluid-exchange of 27% from the measured data and 20% from the simulation, respectively. The histograms shown in Fig. 7 represent the signal distribution within the left extension. In comparison to the histograms shown in Fig. 6, the inflow is more characteristic and a wider distribution of pixels with signals close to one is visible for longer evolution times. On the other hand, T_1 relaxation is clearly visible and approaches $1 - e^{-600/870} \approx 50\%$ of remaining magnetization after 600 ms. The included T_1-fit is fitted to the signal intensities with the highest pixel count and the regression is shown in the histograms, as well. The resulting values fit the 1D measurement of T_1 = 870 ms within the failure tolerance.

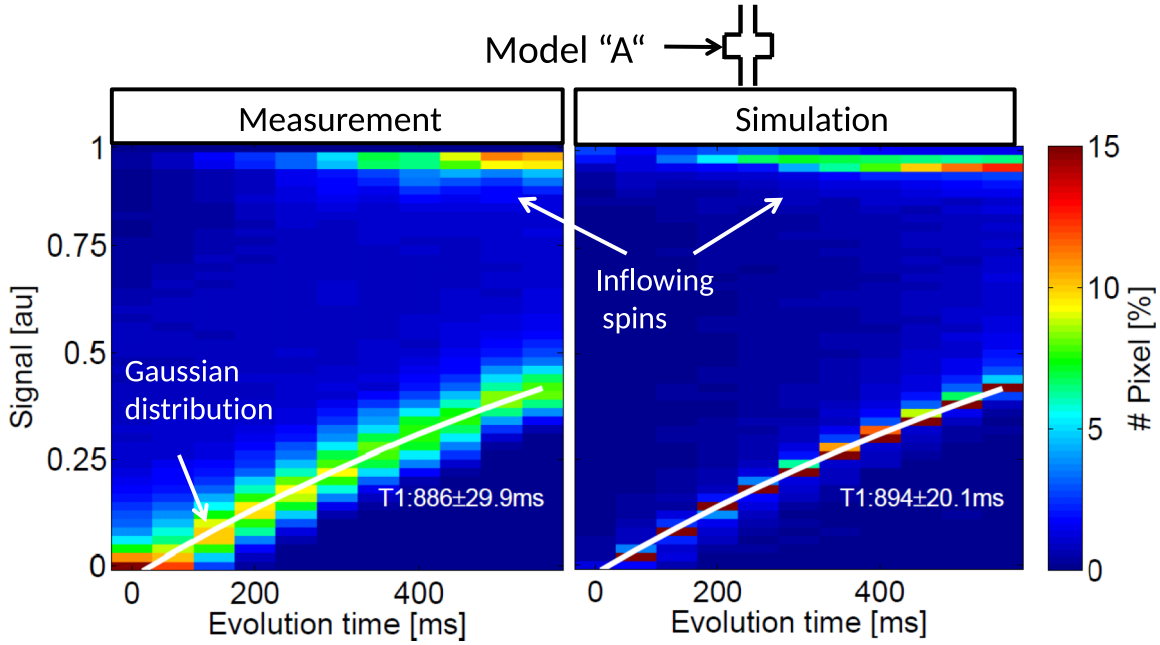

FIG. 7. Histograms of the signal distribution for the left expansion of model A. The left-hand side shows the signal distribution of the measurement while the right-hand side shows the simulation.

4.C.2. Model B—Aneurysm

A visual comparison of the spin transport in Fig. 5 (Multimedia view) shows similar behavior for both measurement and simulation. The unlabeled spins are transported inside the aneurysm at the upper part of the neck and start rotating inward with the resulting vortex (200 ms). After 400 ms, a half-rotation is completed, whereas after 600 ms, the fresh spins have completed a full rotation around the vortex and again start curling inward at a lower radius. The thickness of the visible structures is different in the plots of measurement and simulation. The measured trace of the fresh spins is thicker than in the plot of the simulation; in the latter, the trace is sharper in comparison. While the simulation data are smooth in the aneurysm lumen, noise is visible in the plots of the measurement (SNR = 84). The deviation between measurement and simulation is $(8 \pm 11)\%$ for 200 ms, $(8 \pm 11)\%$ for 400 ms, and $(9 \pm 10)\%$ for 600 ms evolution. A video of the process is presented in the supplementary material. The fluid-exchange is 6% (measurement) and 5% (simulation) after 600 ms. Due to this low fluid-exchange, the measurement cannot trace the spins further because of limitations by the T_1 relaxation. This time can be increased by choosing a different liquid, e.g., pure water ($T_1 \approx 2$ *s*). In the simulation, the T_1 relaxation can be neglected and the mass transport can be analyzed over longer times by tracing the labeled spins leaving the aneurysm lumen. The labeled spins travel asymmetrically with the secondary flow in the vessel alongside the vessel wall; see Fig. 8(b). These observations could not be made in the experiment due to the chosen imaging plane. Additionally, a streamline plot of the resulting simulated velocity field is shown in Fig. 8(a). Here, the streamlines indicate this outflow behavior too, and the low velocities inside the aneurysm as well as the observed vortex are clearly visible.

5. DISCUSSION

The results indicate that the simulated mass transport and spin–lattice relaxation are in good agreement with the experimental results. In model A, the asymmetry in the flow patterns is clearly visible in both methods and the simulation result can be validated. Furthermore, the fluid-exchange can be calculated from both methods, which is helpful information for understanding pathological processes or the functionality of stents. For these purposes, the ToF measurements need a careful setup for choosing useful models in which the method can be used and the tagging sequence must be optimized. The tracking time is limited by the T_1 relaxation, and therefore, the observation time of the fluid-exchange is affected. For a characterization of the flow behavior within the tagged areas, the method is useful. A more time-consuming phase contrast measurement[13] would be a helpful additional method to validate the simulation results.

The multigrid LBM simulations, which were validated in this study, are ideally suited for efficient implementation on asynchronous multi-GPU systems, where locality of the data can be exploited and only limited data have to be transferred. The problem scales almost linearly with the size of the data set. With less than one hour simulation time per model for both grids, accurate simulation results can complement the measurements. Using TRT instead of a SRT model increased the run-time by less than 5%. The improved stability was very noticeable compared to the SRT models.

In the future, we will work on expanding the efficient multigrid multi-GPU simulation presented here toward a simulation of the full Bloch equation for spins in the fluid. Therewith, a simulation of the complete measurement process might be possible, e.g., for analyzing variations in the magnetic field or for quantifying other artifacts and, hopefully, to improve the

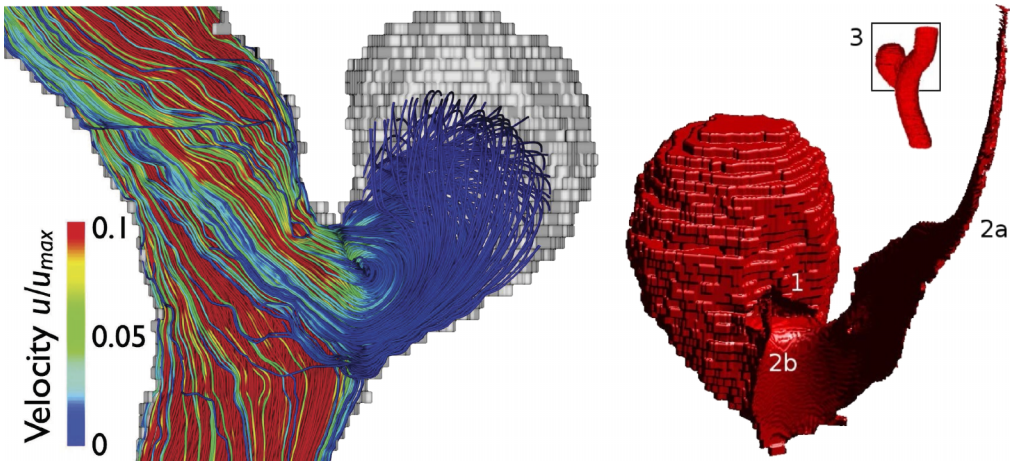

(a) (b)

FIG. 8. (a) Streamline visualization of the velocity field inside of model B aneurysm and part of the vessel. A vortex can be seen where the fluid of the aneurysm lumen touches the fluid of the main flow of the vessel. The maximum velocity of the vortex is ≈1/30 of u_{max} of the vessel. (b) Isosurface visualization of the ToF-labeled spins traveling with the secondary flow inside the vessel part of model B. While the inflow of fresh spins into the aneurysm neck is symmetric (1), the outflow of labeled spins is asymmetric (see differences in 2a, 2b). Small inset (3) at the top right of the figure provides an overview of the viewing angle of the geometry. Flow direction is from bottom to top. The viewing angle in (b) had to be changed because of the asymmetry.

sequences used for imaging. Other aspects like the design of new pulse sequences by optimal control[32] might be incorporated as well.

In the future, we plan to implement more realistic model systems based on pulsatile flow using porcine or human blood.

6. CONCLUSION

In this study, microscopic magnetic resonance flow measurements were used to characterize the fluid-exchange within different aneurysm models. These measurements were used as boundary conditions for the simulation. Furthermore, they were used to validate the LBM flow simulations. The analysis of complex flow patterns using ToF techniques is informative for understanding mass transfer between vessel lumen and aneurysm as well as inside the aneurysm itself. For this purpose, the imaging technique comes close to its limit when observing phenomena in slow-flowing parts of the domain, like the aneurysm lumen opposite to the neck and/or at time scales where signal loss due to T_1 relaxation starts competing with the signal-to-noise ratio.

Using the validated LBM model presented here, we were able to accurately represent mass transport inside the flow domain as well as the T_1 relaxation (which can be turned off). Using a validated simulation helps to understand effects on time scales beyond what spin labeling can capture, such as, simulations are a good complement to experiments.

ACKNOWLEDGMENT

The authors would like to offer their sincerest gratitude to Mercator Research Center Ruhr (MERCUR) for funding this work as part of Project No. PR-2012-0046.

[a]Electronic mail: daniel.edelhoff@tu-dortmund.de
[b]Present address: George-Huntington-Institute, Johann-Krane-Weg 27, Münster 48149, Germany.

[1]E. Hahn, "Detection of sea-water motion by nuclear precession," J. Geophys. Res. **65**, 776–777, doi:10.1029/JZ065i002p00776 (1960).
[2]L. Axel, B. A. Shimakawa, and J. MacFall, "A time-of-flight method of measuring flow velocity by magnetic resonance imaging," Magn. Reson. Imaging **4**, 199–205 (1986).
[3]A. Caprihan and E. Fukushima, "Flow measurements by NMR," Phys. Rep. **198**, 195–235 (1990).
[4]J. Singer, "Blood flow rates by nuclear magnetic resonance measurements," Science **130**, 1652–1653 (1959).
[5]P. Moran, "A flow velocity zeugmatographic interlace for NMR imaging in humans," Magn. Reson. Imaging **1**, 197–203 (1982).
[6]L. F. Gladden and A. J. Sederman, "Recent advances in flow MRI," J. Magn. Reson. **229**, 2–11 (2013).
[7]K. Packer, "Diffusion and flow in fluids," Encycl. Magn. Reson. **1**(3) (2012).
[8]K. Romanenko, D. Xiao, and B. J. Balcom, "Velocity field measurements in sedimentary rock cores by magnetization prepared 3D SPRITE," J. Magn. Reson. **223**, 120–128 (2012).
[9]J. Heverhagen, E. Bourekas, and S. Sammet, "Time-of-flight magnetic resonance angiography at 7 Tesla," Invest. Radiol. **47**, 568–573 (2008).
[10]J. Aguayo, S. Blackband, and J. Schoeniger, "Nuclear magnetic resonance imaging of a single cell," Nature **332**, 190–191 (1986).
[11]Y. Xia, "Imaging the velocity profiles in tubeless siphon flow by NMR microscopy," J. Magn. Reson. **164**, 365–368 (2003).
[12]P. Callaghan, "Velocity and diffusion imaging in dynamic NMR microscopy," J. Magn. Reson. **91**, 326–352 (1991).
[13]D. Edelhoff, L. Walczak, S. Henning, F. Weichert, and D. Suter, "High-resolution MRI velocimetry compared with numerical simulations," J. Magn. Reson. **235**, 42–49 (2013).
[14]S. Henning, D. Edelhoff, B. Ernst, S. Leick, H. Rehage, and D. Suter, "Characterizing permeability and stability of microcapsules for controlled drug delivery by dynamic NMR microscopy," J. Magn. Reson. **221**, 11–18 (2012).
[15]J. R. Brown, T. I. Brox, S. J. Vogt, J. D. Seymour, M. L. Skidmore, and S. L. Codd, "Magnetic resonance diffusion and relaxation characterization of water in the unfrozen vein network in polycrystalline ice and its response to microbial metabolic products," J. Magn. Reson. **225**, 17–24 (2012).
[16]J. Perlo, E. Silletta, E. Danieli, G. Cattaneo, R. Acosta, B. Blümich, and F. Casanova, "Desktop MRI as a promising tool for mapping intra-aneurysmal flow," Magn. Reson. Imaging **33**, 328–335 (2015).
[17]J. Raymond, F. Guillemin, F. Proust, A. J. Molyneux, and A. J. Fox, "Unruptured intracranial aneurysms. A critical review of the international study

of unruptured intracranial aneurysms (ISUIA) and of appropriate methods to address the clinical problem," Interv. Neuroradiol. **14**, 85–96 (2008).
[18]P. van Ooij, A. Guédon, C. Poelma, J. Schneiders, and M. Rutten, "Complex flow patterns in a real-size intracranial aneurysm phantom: Phase contrast MRI compared with particle image velocimetry and computational fluid dynamics," NMR Biomed. **25**, 14–26 (2012).
[19]I. Marshall, S. Zhao, P. Papathanasopoulou, P. Hoskins, and Y. Xu, "MRI and CFD studies of pulsatile flow in healthy and stenosed carotid bifurcation models," J. Biomech. **37**, 679–687 (2004).
[20]Y. Papaharilaou and D. Doorly, "Assessing the accuracy of two-dimensional phase-contrast MRI measurements of complex unsteady flows," J. Magn. Reson. Imaging **723**, 714–723 (2001).
[21]I. Marshall and M. Robertson, "MRI measurement of wall shear stress vectors in bifurcation models and comparison with CFD predictions," J. Magn. Reson. Imaging **14**, 563–573 (2001).
[22]Q. Long, X. Xu, B. Ariff, S. Thom, D. Hughes, and V. Stanton, "Reconstruction of blood flow patterns in a human carotid bifurcation: A combined CFD and MRI study," J. Magn. Reson. Imaging **11**, 299–311 (2000).
[23]K. W. Moser, E. C. Kutter, J. G. Georgiadis, R. O. Buckius, H. D. Morris, and J. R. Torczynski, "Velocity measurements of flow through a step stenosis using Magnetic Resonance Imaging," Exp. Fluids **29**, 438–447 (2000).
[24]A. Haase, J. Frahm, D. Matthaei, W. Hanicke, and K. Merboldt, "FLASH imaging. Rapid NMR imaging using low flip-angle pulses," J. Magn. Reson. **67**, 258–266 (1986).
[25]D. D'Humières, I. Ginzburg, M. Krafczyk, P. Lallemand, and L.-S. Luo, "Multiple-relaxation-time lattice Boltzmann models in three dimensions," Philos. Trans. R. Soc., A **360**, 437–451 (2002).
[26]I. Ginzburg, F. Verhaeghe, and D. d'Humières, "Two-relaxation-time lattice Boltzmann scheme: About parametrization, velocity, pressure and mixed boundary conditions," Commun. Comput. Phys. **3**, 427–478 (2008).
[27]E. G. Flekkøy, "Lattice Bhatnagar-Gross-Krook models for miscible fluids," Phys. Rev. E **47**, 4247–4257 (1993).
[28]I. Ginzburg, "Equilibrium-type and link-type lattice Boltzmann models for generic advection and anisotropic-dispersion equation," Adv. Water Resour. **28**, 1171–1195 (2005).
[29]B. Servan-Camas and F. T.-C. Tsai, "Lattice Boltzmann method with two relaxation times for advection-diffusion equation: Third order analysis and stability analysis," Adv. Water Resour. **31**, 1113–1126 (2008).
[30]I. Ginzburg, D. d'Humières, and A. Kuzmin, "Optimal stability of advection-diffusion lattice Boltzmann models with two relaxation times for positive/negative equilibrium," J. Stat. Phys. **139**, 1090–1143 (2010).
[31]F. Weichert, L. Walczak, D. Fisseler, T. Opfermann, M. Razzaq, S. Turek, R. Münster, I. Grunwald, C. Roth, C. Veith, and M. Wagner, "Simulation of intra-aneurysmal blood flow by using different numerical methods," Comput. Math. Methods Med. **2013**, 527654.
[32]M. Holbach, J. Lambert, and D. Suter, "Optimized multiple-quantum filter for robust selective excitation of metabolite signals," J. Magn. Reson. **243**, 8–16 (2014).

Medical Physics
The International Journal of Medical Physics Research and Practice

Measurement with microscopic MRI and simulation of flow in different aneurysm models

Daniel Edelhoff, Lars Walczak, Frauke Frank, Marvin Heil, Inge Schmitz, Frank Weichert, and Dieter Suter

Citation: Medical Physics **42**, 5661 (2015); doi: 10.1118/1.4929758
View online: http://dx.doi.org/10.1118/1.4929758
View Table of Contents: http://scitation.aip.org/content/aapm/journal/medphys/42/10?ver=pdfcov
Published by the American Association of Physicists in Medicine